Journal of Materials Chemistry A

ROYAL SOCIETY OF CHEMISTRY

PAPER

View Article Online
View Journal | View Issue

Cite this: J. Mater. Chem. A, 2024, 12, 28975

Molecular recognition-induced structural flexibility in ZIF-71†

J. Farrando-Perez,[a] A. Missyul,[b] A. Martín-Calvo,[c] C. Abreu-Jauregui,[a] V. Ramírez-Cerezo,[ad] L. Daemen,[e] Y. Q. Cheng,[e] A. J. Ramirez-Cuesta,[e] S. Calero,[f] C. Carrillo-Carrión[g] and J. Silvestre-Albero*[a]

The adsorption performance of ZIF-71 towards two common volatile organic compounds, chlorobenzene and phenol, has been evaluated using a number of experimental techniques and Grand Canonical Monte Carlo (GCMC) simulations. Experimental results indicate that ZIF-71 can adsorb large quantities of chlorobenzene, while its adsorption performance for a similar molecule, such as phenol, is reduced by one order of magnitude. Synchrotron X-ray powder diffraction patterns confirm the presence of structural changes in ZIF-71 upon exposure to a phenol/water solution, *i.e.*, a phase transition from the open-pore (op) ZIF-71 structure to the narrow-pore (np), highly dense, ZIF-72 phase. Although this phase transition does not occur in the presence of pure water, GCMC simulations suggest that phenol molecules adsorbed at the pore mouth and/or in structural defects may promote water accessibility to the inner core of the ZIF-71 microcrystals, thus promoting this thermodynamically favored phase transition. Inelastic neutron scattering (INS) and neutron diffraction (ND) experiments confirm the ZIF-71 to ZIF-72 phase transition, exclusively in samples exposed to a phenol/water solution. The presence of entrapped water molecules in the inner core of ZIF-71 crystals upon phenol adsorption, even after a drying step, suggests that the phase transition is likely initiated at the external surface of the ZIF-71 crystals.

Received 2nd June 2024
Accepted 18th September 2024

DOI: 10.1039/d4ta03813d

rsc.li/materials-a

Introduction

One of the main challenges the society is facing nowadays is the management of water resources, mainly due to the increasing water scarcity.[1–3] For instance, in the last few years the Mediterranean region has experienced severe droughts, clearly reflected in low river flows, limited dam water reservoirs, and water shortages.[4] According to the World Health Organization (WHO), the water crisis will affect half of the global population by 2025. Under this scenario, wastewater treatment (WWT) becomes crucial to mitigate the problems associated with water scarcity, mainly for agricultural practices and industrial activities. Actual wastewater treatment technologies are based on photocatalytic degradation,[5] advanced oxidation processes,[6] biological WWT,[7] membrane separation and distillation,[8] among others. Among these technologies, adsorption using porous materials (*e.g.*, activated carbon materials, zeolites, metal–organic frameworks, *etc.*) represents a promising approach characterized by its low-cost, high efficiency and ease of operation.[9,10] Zeolitic-imidazolate frameworks (ZIFs), a sub-class of metal–organic frameworks, have emerged as promising adsorbents for the removal of pollutants in wastewater streams with adsorption values above 1000 mg g^{-1}, for cations (*e.g.*, removal of Au(III) in ZIF-8), and above 2000 mg g^{-1}, for industrial dyes (*e.g.*, methylene blue in ZIF-8 or malachite green in MRGO/ZIF).[11–14]

The excellent performance of ZIFs for liquid-phase adsorption processes is mainly attributed to the following factors: (i) high and uniform porosity; (ii) a tunable hydrophilic/hydrophobic character depending on the ZIF type (*i.e.*, hydrophobic ZIF-8 compared to hydrophilic ZIF-90); interestingly, this hydrophilic/hydrophobic balance can be gradually varied by using mixed-linker ZIFs; and (iii) a rich surface chemistry, which can be easily modified using post-synthetic methods for incorporating different functional groups. As a result, ZIF-based adsorbents provide high efficiency for a wide variety of traditional pollutants (*e.g.*, metals, dyes and pesticides), and even for emerging contaminants (*e.g.*, drugs, endocrine disruptors, and plasticizers), whose quantities in water bodies are increasing at an alarming rate and pose significant risks to public health and the environment.[15]

[a]Advanced Materials Laboratory, Department of Inorganic Chemistry-Materials University Institute of Alicante, University of Alicante, E-03690 San Vicente del Raspeig, Spain. E-mail: joaquin.silvestre@ua.es

[b]CELLS – ALBA Synchrotron, Cerdanyola del Vallés, Barcelona, Spain

[c]Center for Nanoscience and Sustainable Technologies (CNATS), Dpt Physical, Chemical and Natural Systems, Universidad Pablo de Olavide, Seville, Spain

[d]Institut Laue-Langevin, 71 avenue des Martyrs, 38000, Grenoble, France

[e]Spallation Neutron Source, Oak Ridge National Laboratory, Oak Ridge, TN 37831, USA

[f]Department of Applied Physics, Eindhoven University of Technology, Eindhoven, The Netherlands

[g]Institute of Chemical Research (IIQ), CSIC – University of Seville, 41092 Seville, Spain

† Electronic supplementary information (ESI) available. See DOI: https://doi.org/10.1039/d4ta03813d

Despite these excellent results described so far, a critical aspect concerns the appearance of potential structural changes in ZIFs under *operando* conditions, *i.e.*, upon liquid-phase adsorption processes. Note that these changes could affect their removal efficiency, limiting their reuse and therefore hindering their true potential in realistic industrial scenarios. Although structural flexibility in ZIFs has been well-documented for gas-phase adsorption processes, to our knowledge these changes have been scarcely explored in liquid-phase adsorption processes, *i.e.*, conditions relevant to water treatment.[16–21] In the presence of an external stimulus (*e.g.*, gas adsorption, temperature, pressure, *etc.*), ZIFs can experience structural dynamics (*e.g.*, gate-opening, breathing, and swelling, among others).[16–22] The identification of these structural changes taking place under *operando* conditions is crucial to understand the mechanism behind adsorption processes in ZIFs, and the existence of selective adsorptions for adsorbates with similar characteristics (*e.g.*, water/alcohol or ethane/ethylene separation processes in ZIFs).[23,24]

With these premises in mind, our main goal in this work is the evaluation of the adsorption performance of a double-chlorinated ZIF material, specifically ZIF-71 (dcim: 4,5-dichloroimidazolate linker), towards two common volatile aromatic organic compounds with similar morphological features (size and shape), but different chemical properties, *i.e.*, phenol and chlorobenzene. Previous theoretical studies by Springer *et al.*[25] have identified that $[Zn(dcim)_2]$-SOD is a very challenging system with a number of hypothetical conformational polymorphs with distinct linker orientations, interconverted *via* reconstructive structural transitions. The effect of these structural characteristics on the adsorption process of two aromatic pollutants, and the concomitant effect of the solvent (aqueous solution) will be thoroughly evaluated through the combined use of synchrotron X-ray diffraction, neutron diffraction and neutron scattering. Experimental findings will be supported by Grand Canonical Monte Carlo simulations.

Experimental section

MOF synthesis

ZIF-71 particles were prepared following the procedure described by Lively *et al.*, with slight modifications.[24] Briefly, a solution of zinc acetate (0.74 g, 4 mmol) in 150 mL of methanol, and a solution of 4,5-dichloroimidazolate (dcIm) (2.19 g, 16 mmol) in 150 mL of methanol, were mixed under stirring conditions for 30 min and left at room temperature (RT) for 24 h. Afterwards, ZIF-71 material was collected by decantation, removing the methanol in the supernatant, and the ZIF-71 particles were then soaked in chloroform (2 × 25 mL) for 2 days. After that, the purified ZIF-71 particles were recovered through filtration, and finally dried under vacuum conditions at 373 K for 24 h.

MOF physicochemical characterization and testing

Nitrogen adsorption isotherms at cryogenic temperatures. Textural properties of the synthesized ZIF-71 particles were evaluated using nitrogen adsorption measurements at 77 K. Gas adsorption measurements were performed in a home-built fully automated manometric setup. Prior to the adsorption measurements, samples were outgassed at 423 K for 12 h under ultra-high vacuum conditions. The specific surface area (S_{BET}) was obtained after the application of the BET equation to the nitrogen adsorption data. Total pore volume was determined from the amount adsorbed at $p/p_0 = 0.97$. Micropore volume (V_{micro}) was obtained by applying the Dubinin–Radushkevich equation (DR) to the nitrogen adsorption data.

Calorimetric measurements. Immersion calorimetry measurements were performed in a SETARAM C-80D calorimeter working at 303 K. A more detailed explanation of the experimental setup can be found elsewhere.[26] For each ZIF-aqueous solution mixture, immersion enthalpy measurements were repeated three times, with a relative standard deviation of less than 5–10% in all cases. Before the immersion analyses, samples were outgassed at 423 K for 12 h under ultra-high vacuum conditions and sealed under vacuum in a specially designed cell.

Thermogravimetric analysis (TGA). Thermogravimetric analyses were performed in a Mettler Toledo TGA/SDTA instrument. To obtain the thermal profiles, an alumina crucible containing 10 mg of sample was heated up to 1248 K under an air flow of 100 mL min^{-1} (heating rate 10 K min^{-1}).

Scanning electron microscopy (SEM). The morphology of the synthesized ZIFs was evaluated using field-emission scanning electron microscopy (FE-SEM). These analyses were performed in a Merlin VP Compact system from ZEISS with a resolution of 0.8 nm at 15 kV and 1.6 nm at 1 kV.

Synchrotron X-ray powder diffraction data (SXRPD). The crystallinity of the ZIF-71 particles was evaluated on the powder diffraction end station of the MSPD beamline at ALBA synchrotron (Spain). Experiments were performed in a capillary reaction cell (fused silica capillary; inner diameter, 0.7 mm; outer diameter, 0.85 mm), using a MYTHEN detector and a wavelength of 0.4138 Å (30 keV), 0.6204 Å (20 keV), and 0.7087 Å (17.5 keV). Measurements were performed on the powdered ZIF-71 materials before and after they were subjected to liquid-phase adsorption processes with the two studied analytes (phenol and chlorobenzene). In these cases, once the liquid-phase adsorption processes reached equilibrium, the samples were filtered and dried at RT for 2 days before performing the synchrotron measurements.

Inelastic neutron scattering (INS) and neutron diffraction (ND) experiments. INS and ND experiments were performed at the VISION beamline of the Spallation Neutron Source (SNS), Oak Ridge National Laboratory (ORNL). A closed cycle refrigerator cryostat was used to control the temperature of the sample in the range of 5–300 K. Samples were treated under the same conditions, as described above for the synchrotron analyses.

Liquid-phase adsorption experiments. The amount of phenol and chlorobenzene adsorbed in ZIF-71 was determined using UV-vis spectroscopy analysis ($\lambda_1 = 270$ nm, for phenol, and $\lambda_2 = 210.6$ nm, for chlorobenzene). Aqueous solutions with initial concentrations of 25, 40, 50, 60, 75, and 100 ppm of phenol, and initial concentrations of 50, 75, 100, 125, 150, 175,

and 200 ppm of chlorobenzene were used for the liquid-phase adsorption tests. In each experiment, 50 mg of ZIF-71 (for phenol experiments), or 15 mg of ZIF-71 (for chlorobenzene experiments), were placed in a vial with 50 mL of each solution and stirred at room temperature until equilibrium was reached (before each experiment, ZIF-71 was outgassed at 423 K overnight). Kinetics studies were performed by taking aliquots at different time intervals and using initial concentrations of 50 ppm and 75 ppm, for phenol and chlorobenzene, respectively. The as-prepared solutions were used without further modification (initial pH = 5.73, for the aqueous chlorobenzene solution, and pH = 5.85, for the aqueous phenol solution). The amount of each analyte adsorbed *vs.* time was quantified by UV-vis spectroscopy using previously obtained calibration curves and the following equation $Q = \frac{(C_0 - C)V}{m}$.

Molecular simulations. Molecular simulations were performed using RASPA software.[27] Adsorption isotherms and radial distribution functions were obtained by performing Monte Carlo simulations in the Grand Canonical ensemble where chemical potential, volume and temperature are kept fixed. Chemical potential was related to pressure through the Peng–Robinson equation. To ensure an equilibrated system, a total of 800 k cycles (with additional 80 k initialization cycles) were used in combination with random moves applied to the molecules (rotation, translation, insertion and deletion). A cycle consists of a maximum of (N,20) attempted moves, where N is the number of molecules. Henry coefficients and heats of adsorption are calculated using the Widom test-particle insertion method.[28] To describe the interactions within the system, Lennard-Jones (L-J) and coulombic potentials are cut and shifted with a cut-off distance of 12 Å. Cross-terms L-J interactions were obtained using Lorentz–Berthelot mixing rules, while the Ewald summation method was used for electrostatic interactions with a relative precision of 10^{-6}.

The structure of the ZIFs was considered rigid and described with the crystallographic atomic positions obtained from the literature.[29] Lennard-Jones parameters were taken from the UFF-universal forcefield,[30] and partial charges were assigned based on the work of Gutierrez-Sevillano *et al.*[31] with a charge of 0.7 e^- assigned to Zn atoms. A detailed list with all the parameters used in this work can be found in Table S1.† Regarding the adsorbates under study, they were all described as full atom rigid models. Atomic positions and point charges for phenol and chlorobenzene were taken from PubChem,[32] while Lennard-Jones parameters were taken from TraPPE.[33] Water was modelled using the extended simple point charge (SPC/E) model.[34] Additionally, pore size distribution (PSD) was computed using the method of Gelb and Gubbins,[35] while the specific surface area (SSA) of the structures was calculated geometrically by "rolling" a helium probe along the surface of the ZIF.[36]

Results and discussion

Textural properties of the synthesized ZIF have been characterized by nitrogen adsorption/desorption measurements at cryogenic temperatures. Fig. 1A shows that ZIF-71 is a purely microporous material with a perfectly sharp knee at low relative pressures (type I isotherm according to the IUPAC classification). This performance is consistent with the predicted cubic symmetry constructed by large α-cages (*ca.* 1.6 nm) connected by eight-/six- and four-membered ring windows.[37] The calculated BET surface area reaches 1063 $m^2\ g^{-1}$, which is in close agreement with the literature.[24] Although this value is slightly smaller than the theoretical surface predicted by our Grand Canonical Monte Carlo calculations (1390 $m^2\ g^{-1}$), it confirms the effective removal of the solvent used in the synthesis, and potential unreacted linkers from the ZIF-71 cavities during the purification steps.[38] The main characteristic of ZIF-71 is the presence of two chlorine atoms in the dcIM linker, functional groups that endow the ZIF-71 material with novel properties compared to the parent ZIF-8 (non-chlorinated counterpart).[24] The pore size distribution obtained after the application of the non-local density functional theory (NLDFT) method to the nitrogen adsorption data reveals two sharp peaks in the microporous range (*ca.* 1.4 and 1.6 nm) attributed to the different cages in ZIF-71, which is in close agreement with theoretical GCMC predictions (Fig. 1B and S1†). Thermogravimetric analysis (Fig. 1C) indicates that ZIF-71 remains stable up to 723 K, with a small weight loss (*ca.* 9–10%), probably due to the removal of some unreacted dcIm molecules entrapped in the pores. Note that the first weight loss occurs at 500 K, a temperature close to the flash point of dcIm (*ca.* 470 K). Above 723 K, the stability of ZIF-71 is lost, observing a gradual decomposition of the framework until complete decomposition occurs at 1200 K. The final inorganic residue after decomposition is 7.5 wt%, most probably corresponding to ZnO. Although ZIFs are considered highly hydrophobic materials, the H_2O adsorption isotherm at 298 K (Fig. 1D) suggests that water vapour can access the porous structure of ZIF-71, preferentially at relatively high humidity values (p/p_0 above 0.8); however, the total amount adsorbed remains very limited (up to 0.35 mmol g^{-1}). The amount of water adsorbed corresponds to 6.3×10^{-3} $cm^3\ g^{-1}$, which is quite small compared to the micropore volume estimated from the nitrogen adsorption data, *i.e.*, 0.35 $cm^3\ g^{-1}$.[24] Scanning electron microscopy images (FE-SEM) confirm the presence of perfectly defined rhombic dodecahedra and cubic crystals, with a size in the micrometer range, *ca.* 1 μm (Fig. 1E).

Upon evaluation of the physicochemical properties of the pristine crystals, ZIF-71 was tested for the liquid-phase adsorption of two volatile organic compounds, phenol and chlorobenzene. These two probe molecules share some similarities such as similar size and shape, although they differ in other physicochemical properties such as polarity, due to the different nature of the functional group (–OH *vs.* –Cl). Fig. 2 shows the adsorption kinetics for (A) phenol and (B) chlorobenzene, for an initial concentration of 50 mg L^{-1} and 75 mg L^{-1}, respectively. At this point it is important to highlight that higher concentrations could not be tested due to the low solubility of these two molecules in water (the hydrophobic nature of the benzene ring contributes to the low solubility).

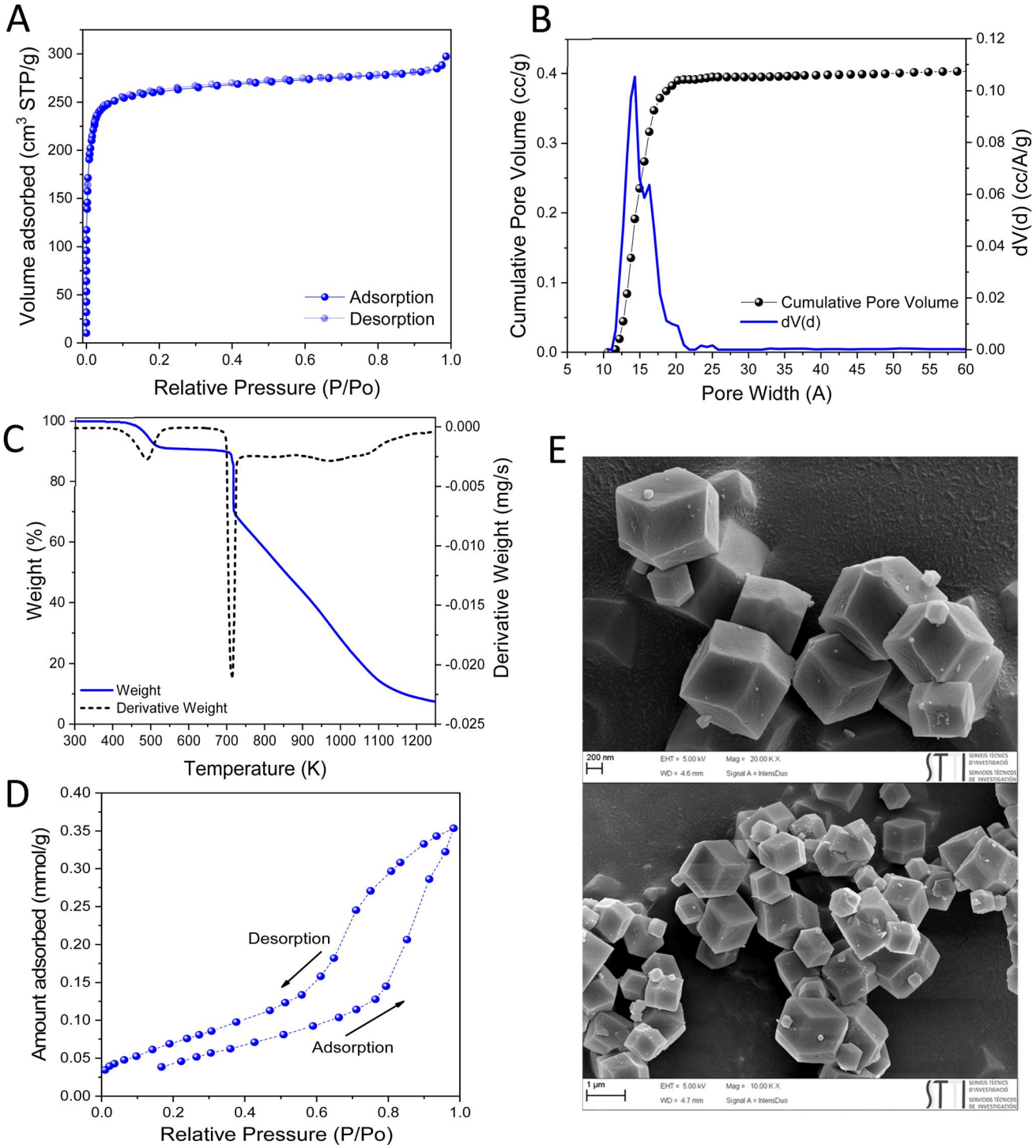

Fig. 1 (A) nitrogen adsorption/desorption isotherm of ZIF-71 at cryogenic temperatures, (B) pore size distribution after application of the NLDFT method to the nitrogen adsorption data (silica, cylindrical pore, equilibrium model), (C) TGA analysis of ZIF-71 in air, (D) water adsorption isotherms at 298 K for ZIF-71, and (E) representative FE-SEM images of the synthesized ZIF-71 microcrystals.

As can be observed in Fig. 2A and B, the adsorption performance of these two molecules differs significantly despite their chemical similarities. While chlorobenzene exhibits fast kinetics (less than 90 min to reach equilibrium), with a total adsorption capacity above 200 mg g^{-1}, phenol needs more than 25 h to reach equilibrium, with a total adsorption capacity an order of magnitude smaller (less than 10 mg g^{-1}). Several repetitions were performed using newly synthesized batches (Fig. S2†). These repetitions confirm that the adsorption kinetics are perfectly reproducible in terms of adsorption capacity (<10% deviation) and adsorption kinetics. Adsorption isotherms (Fig. 2C and D) confirm that the adsorption capacity

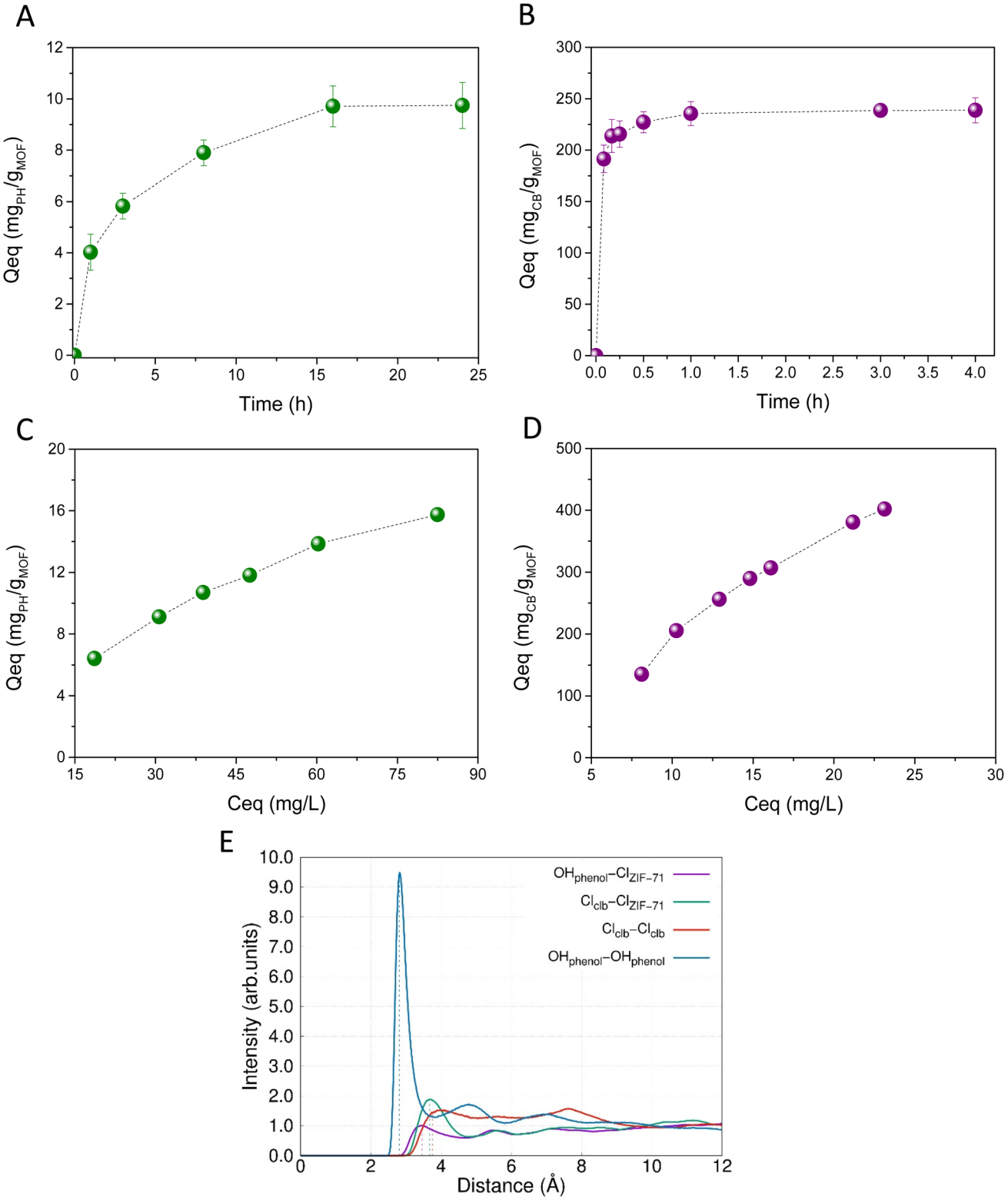

Fig. 2 Adsorption kinetics for (A) phenol ($[C]_0 = 50$ mg L^{-1}, 50 mg ZIF) and (B) chlorobenzene ($[C]_0 = 75$ mg L^{-1}, 15 mg ZIF) in ZIF-71 measured at 298 K, (C and D) liquid-phase adsorption isotherms for phenol and chlorobenzene, respectively, and (E) simulated equilibrium distance between the oxygen and chlorine groups in phenol and chlorobenzene molecules, respectively, and the chlorine functional groups in the ZIF-71 linker (intermolecular distances Cl⋯Cl and HO⋯OH are included for comparison).

at equilibrium for chlorobenzene is one order of magnitude higher compared to that for phenol (*ca.* 16 mg phenol per g_{ZIF71} *vs.* 400 mg chlorobenzene per g_{ZIF71}).

A potential adsorption mechanism to explain the improved adsorption performance for chlorobenzene in ZIF-71 may involve the presence of specific adsorbate–adsorbent interactions between the chlorine-functional group, in chlorobenzene, and the chlorine-groups on the imidazolate linker. Previous studies by Yang *et al.* using fluorinated MOFs showed the presence of F⋯F hydrophobic interactions between a CF_3-functionalized MOF (NH_2-MIL-101 (Fe)) and three fluorinated pesticides, *i.e.*, fipronil, fluazuron and trifluralin, with the associated improvement in the adsorption performance.[39] To ascertain the potential presence of specific Cl⋯Cl interactions responsible for the observed adsorption performance, Grand Canonical Monte Carlo (GCMC) simulations were performed using a rigid ZIF-71 structure. Calculations clearly anticipate a similar accessibility for both molecules to the inner porous structure in ZIF-71, *ca.* 350 mg g^{-1} for both molecules (Fig. S3†). Furthermore, theoretical predictions do not indicate any preferential adsorbent–adsorbate interaction between the chlorine functional groups and chlorobenzene (Fig. 2E and S4†). Intermolecular distances (OH_{phenol}–OH_{phenol}) and (Cl_{CB}–Cl_{CB}) are equal to or smaller than the adsorbent–adsorbate distances (OH_{phenol}–$Cl_{ZIF\text{-}71}$) and (Cl_{CB}–$Cl_{ZIF\text{-}71}$), thus excluding any preferential interaction between the two probes evaluated and the ZIF-71 framework. The heats of adsorption for phenol (−66.6 kJ mol^{-1}) and chlorobenzene (−61.5 kJ mol^{-1}) in ZIF-71 further confirm the absence of preferential adsorbent–adsorbate interactions (Table S2†).

Additional investigations of the effect of chlorobenzene and phenol on the ZIF-71 structure were performed by using synchrotron XRPD. The as-synthesized ZIF-71 presents the cubic symmetry of the RHO topology, as revealed the SXRPD pattern (Fig. 3A). After the liquid-phase adsorption experiment with chlorobenzene, the obtained SXRPD pattern for the treated ZIF-71 is identical to that of the original ZIF-71 (before adsorption), thus ruling out significant structural changes. However, the scenario changes completely for ZIF-71 after the adsorption experiment with phenol. As shown in Fig. 3A, new peaks emerge in the SXRPD pattern, which can be unambiguously assigned to the formation of ZIF-72. The conversion of the porous ZIF-71 phase into the dense, narrow pore, ZIF-72 phase was anticipated by Tu *et al.* when using water vapour as a templating agent during the CVD synthesis of ZIF-71.[40] These studies proved that water vapour can promote this kinetically limited conversion process, giving rise to the thermodynamically stable, highly dense, ZIF-72 structure, whereas other templating agents such as methanol or DMF were not effective. Density functional theory (DFT) calculations predicted a large number of conformational polymorphs for [Zn(dcim)$_2$]-SOD interconverted *via* reconstructive structural transitions.[25] According to these calculations, ZIF-72 was predicted to be more stable than ZIF-71 by 22.3 kJ mol^{-1}. In an attempt to test the potential role of the solvent (liquid water) used in the adsorption processes in the ZIF-71 to ZIF-72 phase transition, similar experiments were performed by exposing ZIF-71 to liquid water under agitation for 24 h at 298 K. The SXRPD pattern shown in Fig. 3B confirms that ZIF-71 retains the original structure upon exposure to liquid water, without any appreciable change. Even a subsequent thermal treatment at 453 K using a conventional oven (aimed to accelerate these kinetically hindered transformations) does not promote the kinetically inhibited conversion process. These observations suggest that either: (i) water does not penetrate in the inner porous structure of ZIF-71, at least to a significant extent when water is used in a liquid form instead of vapors, thus limiting any appreciable structural change, or (ii) the observed changes are exclusively attributed to phenol or the combined role of water/phenol mixtures. Immersion calorimetry measurements were performed in ZIF-71 to estimate the enthalpy of interaction between the ZIF-71 network and the different aqueous solutions tested (pure water, water/phenol and water/chlorobenzene). Fig. S5† reveals the hydrophobic nature of ZIF-71 with a nearly zero immersion enthalpy value, *i.e.*, liquid water cannot wet ZIF-71, or penetrate the inner cavities in a short timescale, whether either alone or in the presence of phenol or chlorobenzene.[41]

To gain further insight into the structural dynamics, ZIF-71 was evaluated using inelastic neutron scattering (INS) at 5 K, before and after the adsorption experiments with phenol and chlorobenzene. Taking advantage of the back detector at the VISION spectrometer, neutron diffraction (ND) data are also reported. The ND pattern of ZIF-71 (Fig. 3C) shows characteristic diffraction peaks that are in close agreement with the theoretical predictions (see model diffraction patterns in the inset). As expected, the ND pattern of ZIF-71 upon chlorobenzene adsorption remains unchanged, thus confirming the high stability of ZIF-71 in the presence of chlorobenzene/water mixtures. However, the scenario changes completely for ZIF-71 upon phenol adsorption in water. Consistent with synchrotron XRPD measurements, ND unambiguously reveals the partial conversion of ZIF-71 into the highly dense ZIF-72 phase. INS is *a priori* a non-useful technique for the evaluation of phase transitions in ZIF-71 due to the perfect matching in the vibrational, librational and rotational modes between ZIF-71 and ZIF-72. As expected, a closer look at the INS spectra in Fig. 3D shows the absence of important changes in the three samples evaluated, *i.e.*, the 0–200 meV region is mainly dominated by N–Zn–N bending and stretching modes, vibrations associated with the Cl atoms, and deformations of the 4-, 6-, and 8-membered rings (MR).[37] However, a careful evaluation of the low energy transfer region provides very useful information about the structural transition mechanism. A comparison between the three spectra unveils slight changes in some characteristic peaks (grey shaded in Fig. 3D) for the ZIF-71 after the adsorption experiment with phenol in water. Unexpectedly, these vibrational contributions do not correspond to phenol adsorbed and/or retained in the inner cavities of the ZIF but rather to water molecules that are entrapped. Translational and librational modes of ice (hexagonal or cubic) are clearly observed. The broad band between 65 meV and 120 meV contains the hindered rotational modes of water molecules, *i.e.* wagging at 69 meV, twisting at 95 meV, and rocking at 115.4 meV. These water molecules seem to be strongly entrapped into the structure, as they were not desorbed during the drying treatment performed after the liquid-phase adsorption experiment, nor

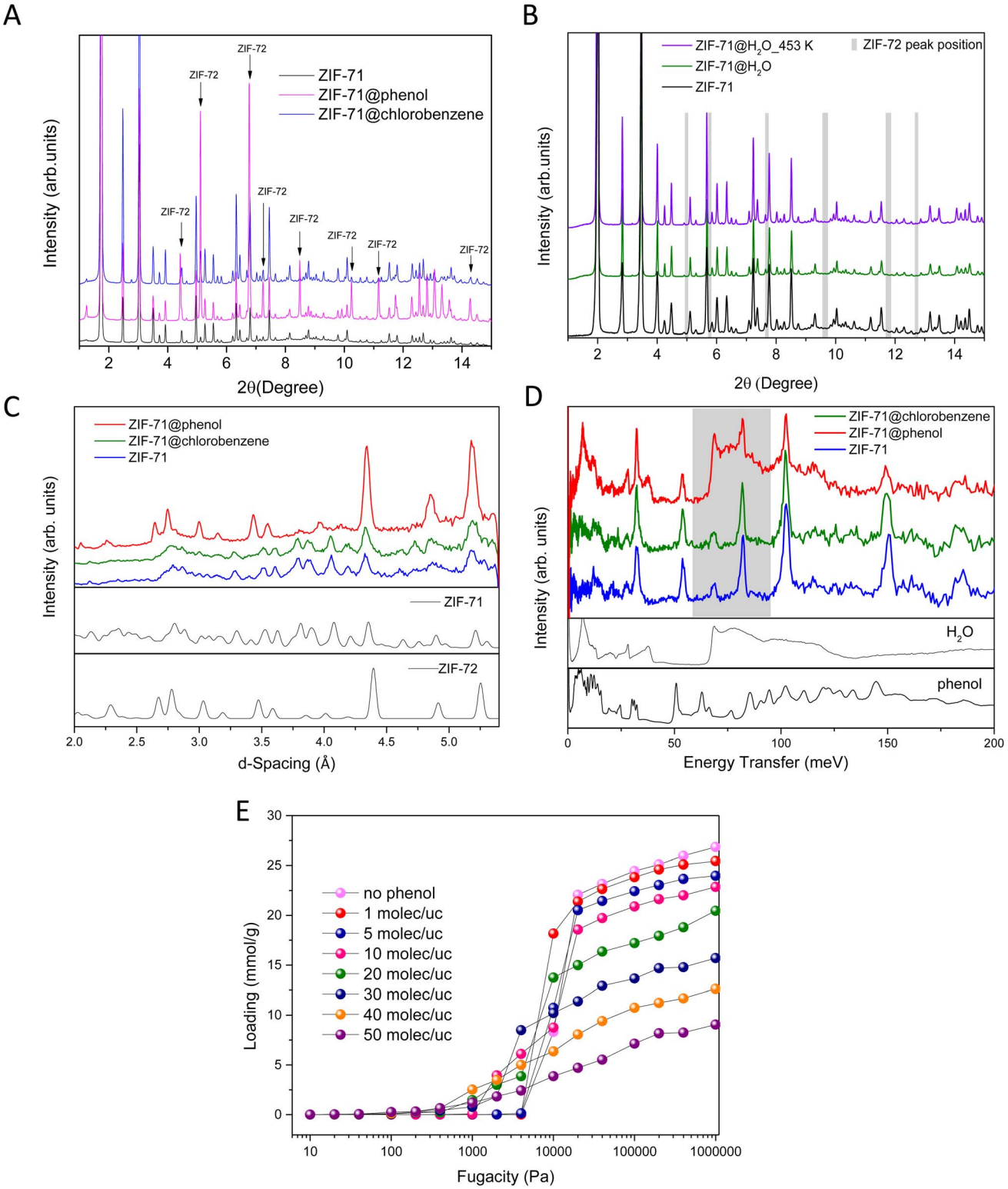

Fig. 3 (A) Synchrotron XRD patterns of the pristine ZIF-71 and the samples after the adsorption of chlorobenzene and phenol (beam energy 20 keV), (B) synchrotron XRD patterns of the pristine ZIF-71 upon exposure to liquid water (simulating the adsorption process) and after a thermal treatment at 453 K upon drying (beam energy 17.5 keV), (C) neutron diffraction (ND) pattern of ZIF-71 before and after the adsorption process with phenol and chlorobenzene. Reference pattern for ZIF-71 and ZIF-72 are included for comparison, (D) inelastic neutron scattering (INS) spectra of ZIF-71 before and after the adsorption process with phenol and chlorobenzene. INS spectra of pure phenol and water are included for the sake of comparison, and (E) simulated water adsorption isotherms at 300 K of ZIF-71 before and after the incorporation of different quantities of phenol molecules in the unit cell.

under the ultra-high vacuum conditions applied at the neutron facilities before the measurements. This finding suggests that in the presence of phenol, liquid water can access the inner porous structure in ZIF-71, thus promoting the phase transition. We can establish several hypotheses to explain these observations, as follows, and it is possible that several factors may contribute to varying degrees (to a greater or lesser extent):

(i) It is well-known in the literature that alcohols promote water accessibility to ZIFs, *i.e.*, less polar alcohols can adsorb at the entrance of ZIF cavities, making these cavities less hydrophobic, thus promoting water accessibility. This effect has been investigated with ethanol/water mixtures.[42]

(ii) Furthermore, water accessibility in these mixtures is also promoted by the large degree of hydrogen bonding between water–phenol pairs (molecular clustering), as compared to water–water pairs in pure water, and the improved packing of water molecules (size entropy effects) inside the cavities.[43]

(iii) On the other hand, it must also be taken into account that not all alcohols have the same properties, and specifically phenol is a weak acid, which is not the case with methanol or ethanol (the most studied alcohols). Note that a solution of phenol in water results in a pH of about 4.5–5.9, depending on the concentration. The vast majority of ZIFs are sensitive to pH, due to the fact that Zn–N bonds can be broken at pH $\leq$ 4.5, and therefore, the acidity of phenol could promote the formation of some structural defects in ZIF-71. These defects could favor water accessibility, and in addition, the open metal sites formed (unsaturated Zn ions) are prone to water coordination.[44] However, the small variations in the pH of the original chlorobenzene and phenol solutions used for these experiments (due to the low concentration) compared to the pH of the distilled water used ruled out the formation of significant structural defects mediated by pH. To further confirm the negligible role of the pH, similar adsorption experiments have been performed under more acidic conditions (pH 3.5; adjusted with a HCl solution). Adsorption kinetics (Fig. S6†) confirm that the total uptake at saturation for phenol and chlorobenzene in ZIF-71 is not altered or modified under acidic conditions, with the exception of a slight increase in the kinetics in the case of phenol. The enhanced kinetics in the case of phenol is consistent with the potential formation of some surface defects at acidic pH. Furthermore, SXRPD analysis of the used samples (Fig. S7†) reveal the absence of ZIF-72 upon chlorobenzene adsorption, while the ZIF-72 phase (*ca.* 15%) is observed after phenol adsorption, which is in close agreement with the experiments described above using non-modified pH conditions.

Looking for some clues to understand how the phenol/water mixture drives the phase transformation from ZIF-71 to ZIF-72, INS suggests that this process is initiated at the external surface of the ZIF-71 microcrystals, and further propagated to the inner core over time. Initiation of the structural transition at the external surface of the ZIF grains will explain the poor adsorption performance of ZIF-71 for phenol (outer shell will be converted after some time to highly dense, narrow-pore, ZIF-72), and the impossibility to remove these water molecules entrapped in the inner cavities of the ZIF, even under UHV conditions. In fact, the pore size aperture in ZIF-72, estimated from the Grand Canonical Monte Carlo simulations, is as low as 0.20 nm (Fig. S1†), smaller than the kinetic diameter of H_2O molecules (*ca.* 0.29 nm). Furthermore, these calculations predict zero adsorption (Fig. S3†) for phenol and chlorobenzene in ZIF-72 (Table S2† also confirms the unfavorable adsorption heats in ZIF-72), in agreement with the limited adsorption capacity observed for phenol in ZIF-71 (Fig. 2A). The highly dense nature of ZIF-72 is also reflected in the low estimated BET surface area (*ca.* 35 $m^2\ g^{-1}$, by GCMC). Most probably, water molecules that penetrate the inner porous structure of ZIF-71, an accessibility process promoted by phenol pre-adsorbed at the pore entrance and/or phenol-induced defects, promote the ZIF-71 to ZIF-72 transition at the outer layers, leaving pre-adsorbed water molecules entrapped within the core of the micron-sized particles (Fig. 1E). Most probably, these entrapped water molecules prevent the complete phase transition. A similar phase transition was described by Mortada *et al.* in ZIF-71-LiCl 20 M aqueous solutions during water intrusion–extrusion experiments at high pressures (*ca.* 200 MPa).[45] The strong capillary forces exerted by adsorbed water molecules must be responsible for these structural changes.[46] To further understand the role of phenol in the adsorption process, water adsorption isotherms have been simulated using GCMC for both the original ZIF-71 structure, and the same ZIF modified with different contents of phenol (1, 5, 10, 20, 30, 40 and 50 molecules per unit cell). Simulated water isotherms at 300 K (Fig. 3E) confirm that the presence of phenol inside the crystals promote water adsorption at lower relative pressures (low fugacity). These findings would agree with INS results, *i.e.*, phenol plays a promoting role in enhancing water accessibility to the inner core of the ZIF-71 crystals, the entrapped water (capillary forces) and/or the generated surface defects are responsible for this phase transition. Synchrotron XRPD measurements (Fig. S8†) also confirm the presence of entrapped water molecules in the ZIF-71 structure, exclusively after the phenol adsorption experiments (appearance of a low 2θ peak at 1.2°). At this point it is important to highlight that similar experiments (not shown) using methanol as a solvent instead of water reflect a poor adsorption performance for both phenol and chlorobenzene with no structural changes observed.

To further understand the kinetically limited ZIF-71 to ZIF-72 phase transition, ZIF-71 samples upon adsorption and drying were thermally treated at 453 K. As shown above (Fig. 3B), heating the ZIF-71 material at 453 K following exposure to liquid water for 24 h does not promote any phase transition to the thermodynamically stable ZIF-72 structure. In the specific case of the ZIF-71 sample used for phenol adsorption, synchrotron XRPD patterns (Fig. S8†) confirm the formation of ZIF-72, and the extent of this phase transition (ZIF-71 into ZIF-72) is promoted at high temperature (*i.e.*, once the phase transition is initiated, high temperatures favor the irreversible kinetically restricted transition process). For the ZIF-71 sample used in chlorobenzene adsorption experiments, after the adsorption process the amount of ZIF-72 formed is negligible (Fig. S9†), and this phase transition increases only minimally after a high temperature treatment. In other words, the ZIF-71 to ZIF-72 phase transition requires the formation of some ZIF-72 nuclei, promoted by water, so that the whole process can be kinetically accelerated at high temperatures. Without these nucleation

points, ZIF-71 remains stable under a thermal treatment at 453 K. FE-SEM images (Fig. S10†) of the ZIF-71 particles after the phase transition (induced by phenol/water mixtures and a subsequent thermal treatment at 453 K) show that the morphology of the original particles is retained, although some defects can be observed in some crystals, most probably due to the forced desorption of entrapped water molecules at 453 K. To gain some insights into the transition mechanism, whether it is solid–solid phase transition or a dissolution/precipitation mechanism, additional experiments have been performed by exposing ZIF-71 to the vapors of an aqueous solution of phenol (50 ppm) for 5 h. SXRPD patterns in Fig. S11† show the complete conversion of ZIF-71 to ZIF-72 (100% conversion), thus excluding any dissolution/precipitation mechanism.

In summary, these results disclose that ZIF-71 experience a phase transition from the open network to a highly dense, narrow-pore ZIF-72 polymorph. This phase transition is irreversible and highly sensitive to the nature of the probe molecule to be adsorbed and the solvent used. Apparently, the phase transition is promoted once water molecules penetrate the inner porous structure of pristine ZIF-71. The kinetically limited phase transition is enhanced at high temperatures, but only when ZIF-72 domains have already formed during the adsorption process. The unit cell contraction after the phase transition is as high as 35.4% (Table S3†), from the original open-pore ZIF-71 (unit cell parameter, $a = 28.6121$ Å; $V = 23423.36$ Å^3, $d = 1.141$ g cm^{-3}), to the narrow-pore ZIF-72 (unit cell parameter, $a = 19.6290$ Å; $V = 7563.01$ Å^3, $d = 1.777$ g cm^{-3}). The refined patterns for some of the evaluated samples are summarized in Fig. S12.† At this point it is important to highlight that contribution of phenol or chlorobenzene to the SXRPD patterns is negligible, probably due to the small adsorption capacity (in the case of phenol) and/or to the random orientation of the adsorbed molecules in the pores with poor contribution to the diffraction maxima (in the case of chlorobenzene). Fractional coordinates of Zn atoms were included in the refinement, but their variation from one sample to another is negligible, thus ruling out the presence of significant structural defects.[46] The percentage of ZIF-71 converted to ZIF-72 shown in Table S3† (upon exposure to phenol/water mixtures) is an average value since this is a kinetically restricted process and it was difficult to reproduce the values when comparing different batches (although adsorption kinetics were perfectly reproducible – Fig. S2†). Even small quantities of ZIF-72 (<5%) could be observed in two out of five batches evaluated with the ZIF-71 exposed to chlorobenzene/water mixtures.

Conclusions

This study confirms that ZIFs can also experience structural changes during liquid-phase adsorption processes, similar to those described for gas adsorption processes. However, in the case of liquid-phase processes, the structural changes highly depend on the nature of the probe molecule to be removed, the nature of the solvent and the synergetic effects between them. In the specific case of ZIF-71, synchrotron X-ray powder diffraction measurements confirm the occurrence of a phase transition to the highly dense, narrow pore, ZIF-72 structure, preferentially in the presence of phenol/water mixtures. Similar experiments with chlorobenzene/water do not promote these structural changes, at least not to a significant extent. Inelastic neutron scattering measurements indicate that this phase transition is initiated in the external layers of the microcrystals (shell-to-core process), promoted by water molecules wetting the inner cavities. GCMC simulations confirm that phenol pre-adsorbed at the pore mouth or in structural defects of ZIF-71 may promote water accessibility to the inner porous structure, thus promoting the structural densification.

Data availability

Our data are available at the RUA repository under this link: **https://hdl.handle.net/10045/146938**.

Author contributions

J. Farrando-Perez: investigation, data curation, writing – original draft; A. Missyul: investigation, data curation, writing – review & editing; A. Martin-Calvo: investigation, data curation, writing – original draft; C. Abreu-Jauregui: investigation; V. Ramirez-Cerezo: investigation; L. Daemen: investigation; Y. Q. Cheng: data curation; A. J. Ramirez-Cuesta: data curation; S. Calero: methodology, supervision, writing – review & editing; C. Carrillo-Carrión: writing-original draft; J. Silvestre-Albero: conceptualization, methodology, funding acquisition, supervision, writing – original draft, writing – review & editing.

Conflicts of interest

There are no conflicts to declare.

Acknowledgements

J. S. A. acknowledges financial support from MCIN (Project PID2022-142960OB-C21), and Conselleria de Innovación, Universidades, Ciencia y Sociedad Digital, Generalitat Valenciana (Project CIPROM/2021/022). Synchrotron X-ray powder diffraction measurements were performed at the Spanish ALBA synchrotron (Projects AV-2023027577 and AV-2022097149). INS experiments were conducted at the VISION beamline (Project IPTS-29742.1) at the Spallation Neutron Source, Oak Ridge National Laboratory (ORNL), which is supported by the Scientific User Facilities Division, Office of Basic Energy Sciences (BES), US Department of Energy (DoE), under contract no. DE-AC0500OR22725 with UT Battelle, LLC. A.M.-C. thanks MCINyU (IJC2019-042207-I) and C3UPO for financial and HPC support. V. R. C. acknowledges a PhD fellowship from ILL (project CLAHY2).

References

1 A. Jodar-Abellan, P. Fernandez-Aracil and J. Melgarejo-Moreno, *Water*, 2019, **11**, 1009.
2 J. Martínez-Valderrama, G. Del Barrio, M. E. Sanjuán, E. Guirado and F. T. Maestre, *Land*, 2022, **11**, 272.

3 *Water, Agriculture and the Environment in Spain: can we square the circle?*, ed. L. De Stefano and M. Ramón Llamas, CRC Press, 2013.
4 J. Albiac, E. Esteban, J. Tapia Barcones and E. Rivas, Water scarcity and droughts in Spain: Impacts and policy measures, in "*Drought in arid and semi-arid regions. A multi-disciplinary and cross-country perspective*", ed. K. Schwabe, J. Albiac, J. D. Connor, R. M. Hassan and L. Meza Gonzalez, Springer Science 2013.
5 C. Abreu-Jauregui, L. Andronic, A. Sepulveda-Escribano and J. Silvestre-Albero, *Environ. Res.*, 2024, **251**, 118672.
6 B. Bethi, S. H. Sonawane, B. A. Bhanvase and S. P. Gumfekar, *Chem. Eng. Process.*, 2016, **109**, 178–189.
7 L. Machineni, *Water Sci. Technol.*, 2019, **80**, 2013–2026.
8 B. van Der Bruggen, *Ind. Eng. Chem. Res.*, 2013, **52**, 10335–10341.
9 M. S. Ali, J. T. Orasugh, S. Sinha Ray and D. Chattopadhyay, Wastewater remediation for reuse through emerging technologies, in *Development in Wastewater Treatment Research and Processes*, Elsevier Inc., 2023, pp. 61–67.
10 S. Feijoo, M. Kamali and R. Dewil, *Chem. Eng. J.*, 2023, **455**, 140589.
11 J. O. Ighalo, S. Rangabhashiyam, C. A. Adeyanju, S. Ogunniyi, A. G. Adeniyi and C. A. Igwegbe, *J. Ind. Eng. Chem.*, 2022, **105**, 34–48.
12 Y. Feng, Y. Li, M. Xu, S. Liu and J. Yao, *RSC Adv.*, 2016, **6**, 109608–109612.
13 K.-Y. A. Lin and W.-D. Lee, *Appl. Surf. Sci.*, 2016, **361**, 114–121.
14 C. Hu, W. Xu, X. Mo, H. Li, S. Zhou, P. Zhang and K. Tang, *Adsorption*, 2018, **24**, 733–744.
15 A. Nalaparaju and J. Jiang, *Adv. Sci.*, 2021, **8**, 2003143.
16 P. Zhao, S. C. E. Tsang and D. Fairen-Jimenez, *Cell Rep. Phys. Sci.*, 2021, **2**, 100544.
17 A. Scheemann, V. Bon, I. Schwedler, I. Senkovska, S. Kaskel and R. A. Fischer, *Chem. Soc. Rev.*, 2014, **43**, 6062–6096.
18 M. E. Casco, Y. Q. Cheng, L. L. Daemen, D. Fairen-Jimenez, E. V. Ramos-Fernandez, A. J. Ramirez-Cuesta and J. Silvestre-Albero, *Chem. Commun.*, 2016, **52**, 3639–3642.
19 J. Gandara-Loe, A. Missyul, F. Fauth, L. L. Daemen, Y. Q. Cheng, A. J. Ramirez-Cuesta, P. I. Ravikovitch and J. Silvestre-Albero, *J. Mater. Chem. A*, 2019, **7**, 14552–14558.
20 N. Talukder, Y. Wang, B. B. Nunna, X. Tong and E. S. Lee, *Microporous Mesoporous Mater.*, 2024, **366**, 112934.
21 D. Fairen-Jimenez, S. A. Moggach, M. T. Wharmby, P. A. Wright, S. Parsons and T. Düren, *J. Am. Chem. Soc.*, 2011, **133**, 8900–8902.
22 S. A. Moggach, T. D. Bennett and A. K. Cheetham, *Angew. Chem., Int. Ed.*, 2009, **48**, 7087–7089.
23 Y. Wu, H. Chen, D. Liu, Y. Qian and H. Xi, *Chem. Eng. Sci.*, 2015, **124**, 144–153.
24 R. P. Lively, M. E. Dose, J. A. Thompson, B. A. McCool, R. R. Chance and W. J. Koros, *Chem. Commun.*, 2011, **47**, 8667–8669.
25 S. Springer, I. A. Baburin, T. Heinemeyer, J. G. Schiffmann, L. van Wüllen, S. Leoni and M. Wiebcke, *CrystEngComm*, 2016, **18**, 2477–2489.
26 J. Silvestre-Albero, C. Gómez de Salazar, A. Sepúlveda-Escribano and F. Rodríguez-Reinoso, *Colloids Surf., A*, 2001, **187–188**, 151–165.
27 D. Dubbeldam, S. Calero, D. E. Ellis and R. Q. Snurr, *Mol. Simul.*, 2016, **42**, 81–101.
28 B. Widom, *J. Chem. Phys.*, 1963, **39**, 2808–2812.
29 R. Banerjee, A. Phan, B. Wang, C. Knobler, H. Furukawa, M. O'Keeffe and O. M. Yaghi, *Science*, 2008, **319**, 939–943.
30 A. K. Rappe, C. J. Casewit, K. S. Colwell, W. A. Goddard III and W. M. Skiff, *J. Am. Chem. Soc.*, 1992, **144**, 10024–10035.
31 J. J. Gutierrez-Sevillano, S. Calero, C. O. Ania, J. B. Parra, F. Kapteijn, J. Gascon and S. Hamad, *J. Phys. Chem. C*, 2013, **117**, 466–471.
32 S. Kim, J. Chen, T. Cheng, A. Gindulyte, J. He, S. He, Q. Li, B. A. Shoemaker, P. A. Thiessen, B. Yu, L. Zaslavsky, J. Zhang and E. E. Bolton, *Nucleic Acids Res.*, 2023, **51**, D1373–D1380.
33 N. Rai and J. I. Siepmann, *J. Phys. Chem. B*, 2013, **117**, 273–288.
34 H. J. C. Berendsen, J. R. Grigera and T. P. Straatsma, *J. Phys. Chem.*, 1987, **91**, 6269–6271.
35 L. D. Gelb and K. E. Gubbins, *Langmuir*, 1999, **15**, 305–308.
36 T. Düren, F. Millange, G. Férey, K. S. Walton and R. Q. Snurr, *J. Phys. Chem. C*, 2007, **111**, 15350–15356.
37 A. F. Möslein and J.-C. Tan, *J. Phys. Chem. Lett.*, 2022, **13**, 2838–2844.
38 W. Morris, B. Leung, H. Furukawa, O. K. Yaghi, N. He, H. Hayashi, Y. Houndonougbo, M. Asta, B. B. Laird and O. M. Yaghi, *J. Am. Chem. Soc.*, 2010, **132**, 11006–11008.
39 C. Yang and Y. Xia, *ACS Appl. Nano Mater.*, 2022, **5**, 5268–5277.
40 M. Tu, D. E. Kravchenko, B. Xia, V. Rubio-Gimenez, N. Wauteraerts, R. Verbeke, I. F. J. Vankelecom, T. Stassin, W. Egger, M. Dickmann, H. Amenitsch and R. Ameloot, *Angew. Chem., Int. Ed.*, 2021, **60**, 7553–7558.
41 C. Cuadrado-Collados, C. K. Rojas-Mayorga, B. Saavedra, M. Martinez-Escandell, J. M. Osinski, P. Moghadam, D. Fairen-Jimenez and J. Silvestre-Albero, *J. Phys. Chem. C*, 2019, **123**, 11699–11706.
42 J. Cousin-Saint-Remi and J. F. M. Denayer, *Chem. Eng. J.*, 2017, **324**, 313–323.
43 R. Krishna and J. M. van Baten, *ACS Omega*, 2020, **5**, 28393–28402.
44 M. E. A. Safy, M. Amin, R. R. Haikal, B. Elshazly, J. Wang, Y. Wang, C. Wöll and M. H. Alkordi, *Chem.–A Euro. J.*, 2020, **26**, 7109–7117.
45 B. Mortada, G. Chaplais, H. Nouali, C. Marichal and J. Patarin, *J. Phys. Chem. C*, 2019, **123**, 4319–4328.
46 J. Liu, J. L. Prelesnik, R. Patel, B. V. Kramar, R. Wang, C. D. Malliakas, L. X. Chen, J. I. Siepmann and J. T. Hupp, *J. Am. Chem. Soc.*, 2023, **145**, 27975–27983.

